Luminescent Gold Nanoclusters Interacting with Synthetic and Biological Vesicles

Regina M. Chiechio, Solene Ducarre, Grégory Moulin, Aurelien Dupont, Célia Marets, Pascale Even-Hernandez, Franck Artzner, Paolo Musumeci, Giorgia Franzò, Célia Ravel, et al.

THE JOURNAL OF PHYSICAL CHEMISTRY LETTERS
A JOURNAL OF THE AMERICAN CHEMICAL SOCIETY

pubs.acs.org/JPCL

Letter

Luminescent Gold Nanoclusters Interacting with Synthetic and Biological Vesicles

Regina M. Chiechio, Solène Ducarre, Grégory Moulin, Aurélien Dupont, Célia Marets, Pascale Even-Hernandez, Franck Artzner, Paolo Musumeci, Giorgia Franzò, Célia Ravel, Maria José LoFaro, and Valérie Marchi*

Cite This: *J. Phys. Chem. Lett.* 2022, 13, 6935–6943

Read Online

ACCESS | Metrics & More | Article Recommendations | Supporting Information

ABSTRACT: According to their high electron density and ultrasmall size, gold nanoclusters (AuNCs) have unique luminescence and photoelectrochemical properties that make them very attractive for various biomedical fields. These applications require a clear understanding of their interaction with biological membranes. Here we demonstrate the ability of the AuNCs as markers for lipidic bilayer structures such as synthetic liposomes and biological extracellular vesicles (EVs). The AuNCs can selectively interact with liposomes or EVs through an attractive electrostatic interaction as demonstrated by zetametry and fluorescence microscopy. According to the ratio of nanoclusters to vesicles, the lipidic membranes can be fluorescently labeled without altering their thickness until charge reversion, the AuNCs being located at the level of the phosphate headgroups. In presence of an excess of AuNCs, the vesicles tend to adhere and aggregate. The strong adsorption of AuNCs results in the formation of a lamellar phase as demonstrated by cryo-transmission electron microscopy and small-angle X-ray scattering techniques.

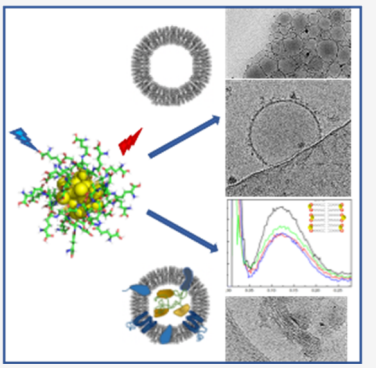

Gold nanoclusters (AuNCs) make up a recently identified class of nontoxic fluorophores. Their brightness, ultrasmall size (<2 nm), large fluorescence lifetime window (1 ns to 1 μs), and good biocompatibility make them an attractive alternative as fluorescent probes for biological labeling and bioimaging.[1−3] Their size approaches the Fermi wavelength of electrons between metal atoms and nanoparticles. It results in molecule-like properties, including discrete energy levels and size-dependent fluorescence of the specific electronic structures. Because of its high electron density, the presence of the gold element can be detected by high-resolution electron microscopy imaging. In addition, their ultrasmall size facilitates their clearance when they are injected into the body. In particular, gold nanoclusters can be filtered from the kidney and urinary excretion rapidly, subsequently reducing their level of accumulation in the liver or spleen.[4−6] Multifunctional nanoconjugates based on AuNCs have been applied in tumor imaging.[7,8]

Understanding their interactions with biological membranes is directly relevant to evaluating nanotoxicity, conceiving the design of nanoparticle vectors or biosensors, and controlling biological membrane targeting. In addition to the advantageous biocompatibility and ease of preparation, the AuNCs have large Stokes shifts and long lifetimes, and hence, they become attractive materials for developing sensitive sensing for various analytes such as heavy metal ions, small biomolecules, and proteins.[9] AuNCs could serve as membrane biomarkers[10,11] or building blocks for nanovector design.[12,13] Gold nanoclusters have been used to track and visualize breast cell-derived extracellular vesicles (EVs) in their parent cells from early endocytosis and lysosomal degradation. They were also found to self-assemble with EVs to form larger defined supraparticles.[14] Due to the viscoelastic properties of lipid membranes, interacting nanoparticles can induce membrane deformation if the attractive interaction is strong enough to balance the energetic bending cost.[13] For example, electrostatically interacting quasi-spherical quantum dots[15] or nanorods[16] can deform model membranes into egg box-like structured lamellae or corrugated sheets. Recently, the size dependence of electrostatic interactions between gold nanoparticles (with a diameter between 5 and 40 nm) has been demonstrated.[17] This study shows that the smaller the particles are, the more they can induce a strong deformation of the membrane.

Here we investigate the interaction between biocompatible luminescent AuNCs (with a diameter of <2 nm) and synthetic liposomes of different sizes (with a diameter between 20 nm and 10 μm approximatively) or biological human EVs. EV is the generic term for particles naturally released from the cell

Received: April 12, 2022
Accepted: July 13, 2022
Published: July 25, 2022

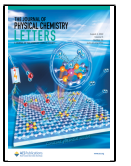

https://doi.org/10.1021/acs.jpclett.2c01071
J. Phys. Chem. Lett. 2022, 13, 6935−6943

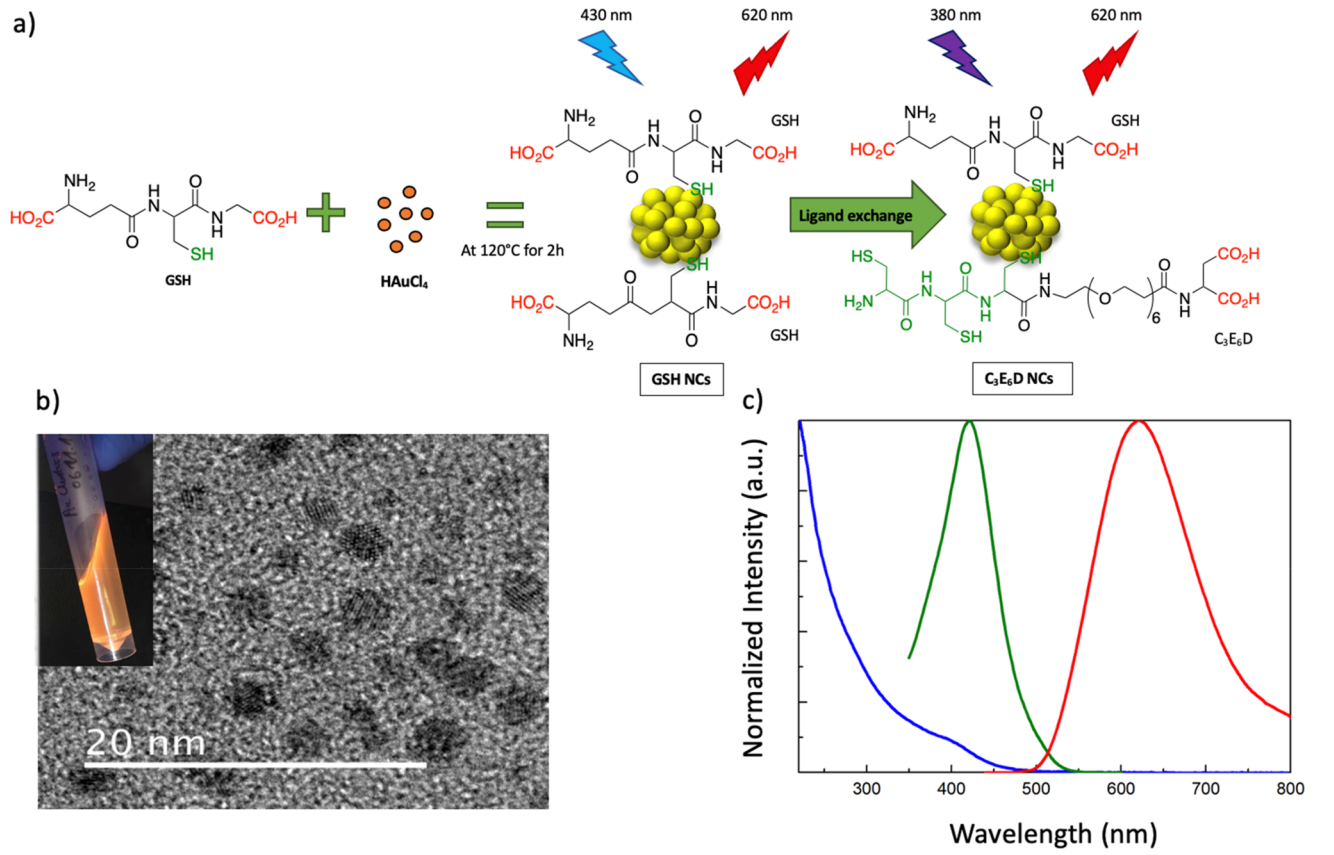

Figure 1. (a) Schematic view of the synthesis of glutathione (GSH) gold nanoclusters followed by ligand exchange. (b) High-resolution TEM images of GSH Au NCs. Scale bar, 20 nm. GSH Au NC solution under an ultraviolet lamp in the inset. (c) Optical properties of GSH Au NCs: (blue) ultraviolet−visible spectrum, (green) normalized excitation spectrum (620 nm), and (red) normalized fluorescence emission spectrum (430 nm).

that are delimited by a lipid bilayer without any functional nucleus. These vesicles are membrane-limited particles that are secreted by healthy and cancerous cells. EVs are heterogeneous in size, and three subtypes are described depending on the location of secretion: microvesicles, myelinosomes, and exosomes.[18,19] A specific human fluid particularly rich in extracellular vesicles was selected to better understand the mechanism of their interaction with AuNCs. Indeed, EVs are identified in follicular fluid as a mode of communication in the ovarian follicle.[20] In addition, EVs involved in cell−cell communication are considered as biomarkers for early cancer diagnosis.[21−25] Their labeling with easily detectable nanoparticles could enable the development of a powerful tool for the early diagnosis of specific diseases.

We first synthesize biocompatible luminescent positively (AuNC+) or negatively (AuNC−) charged gold nanoclusters. We choose the strong and long-range electrostatic interaction to magnify any possible interaction with the membrane. The AuNCs of various surface charges were synthesized in two steps: (1) synthesis of glutathione-stabilized AuNCs according to the literature[26] by using a higher temperature to accelerate its kinetics and (2) a ligand exchange with PEGylated peptides with a high affinity for the gold surface.[27] Typically, a solution containing the glutathione reductant (GSH) and gold(III) salts was heated at its boiling point for 2 h to obtain the GSH NC suspension (Figure 1a). The analysis of the transmission electron microscopy (TEM) images (Figure 1b) reveals the crystalline structure of the NCs and their ultrasmall dimensions with a diameter of 1−2 nm. Due to quantum confinement,[28,29] the NCs do not have the collective plasmon excitation typical of nanoparticles (NPs) and have composition- and size-dependent fluorescence properties. As expected, the GSH NCs exhibit a maximum of fluorescence intensity at 620 nm (Figure 1c). The excitation spectrum exhibits a typical peak corresponding to the Au atom excitation with a maximum at 410 nm (Figure 1c). The absorption spectrum presents a strong absorption due to the scattering below 350 nm masking the absorption peak of the AuNC.

The diameter size histogram obtained by analysis of the TEM images presents a rather small polydispersity around 2 nm (1.2−2.4 nm). The fluorescence lifetime measurements exhibit a better fit using two exponential decays (Figure S1) corresponding to two lifetimes (τ_1 = 3.1 ± 0.02 μs, and τ_2 = 0.67 ± 0.02 μs). This observation could be attributed to two different emission processes from the surface (ligand−metal interaction) or from the AuNC core.[30] Even after lyophilization, the AuNCs are very easy to resuspend in water without any detectable aggregation or loss of luminescence (Figure S2).

To increase the colloidal stability of AuNCs, three cysteine PEGylated peptides that are negatively (C_3E_6D and C_5PEG_4) or positively charged (K_5CNH_2) (see Figure S3) were selected for their high ligand affinity according to our previous works.[31,32] In this study, we also successfully used the commercial positively charged MUTAB (mercapto-undecyl-trimethyl ammonium bromide) compound as an alternative to the K_5CNH_2 compound. It is noticeable that the MUTAB single thiolate ligand with a permanent trimethylammonium charge regardless of pH is suitable for only in vitro experiments

https://doi.org/10.1021/acs.jpclett.2c01071
J. Phys. Chem. Lett. 2022, 13, 6935−6943

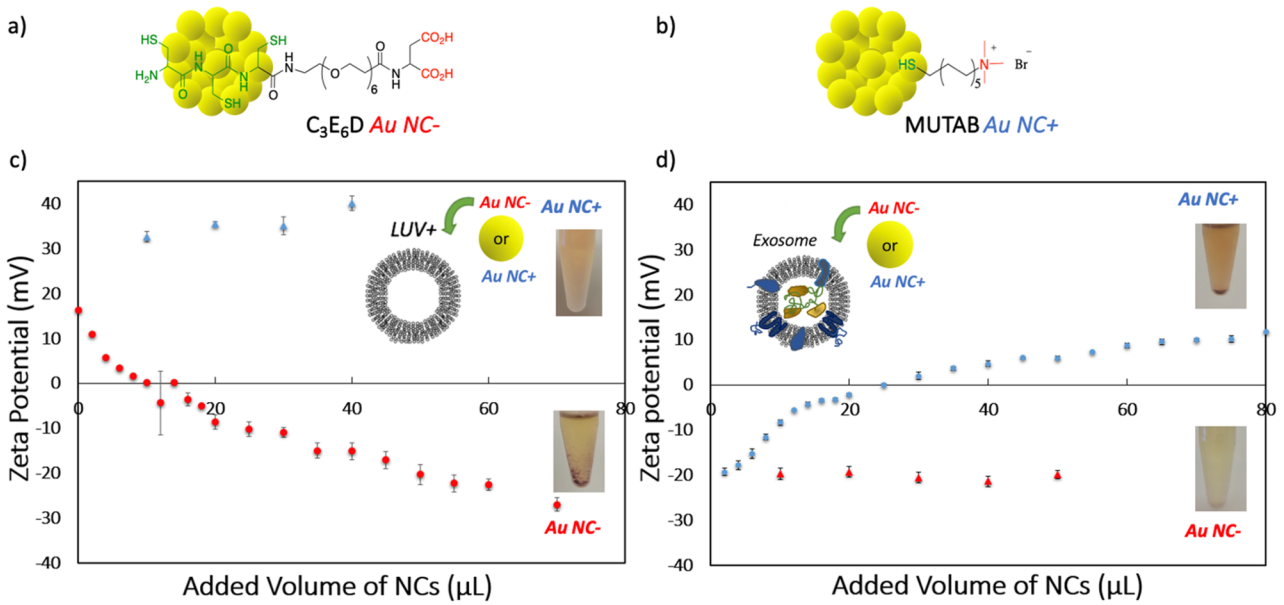

Figure 2. Schematic structure of ligand-exchanged (a) negatively charged C_3E_6D AuNC− (red) and (b) positively charged MUTAB AuNC+ (blue). (c) Evolution of the ζ potential during the titration of positively charged 9:1 DOPC/DOTAP large unilamellar vesicle liposomes (total lipid concentration of 1 mM) with negatively charged C_3E_6D AuNC− (red) or positively charged MUTAB AuNC+ (blue). (d) Evolution of the ζ potential during the titration of negatively charged exosomes with negatively charged C_3E_6D AuNC− (red) and positively charged MUTAB AuNC + (blue).

because of its potential toxicity. The ligand exchange allows us to obtain nanoclusters with a higher biocompatibility and stability against aggregation in aqueous buffer media due to the presence of the PEG and the terminal charges of the aspartic carboxylate or ammonium groups. The C_3E_6D NCs can also be bioactivated through binding of a functional targeting group (antibodies, recognition proteins, and drugs) to the terminal carboxylic groups for further diagnostic and therapeutic applications. After overnight incubation in the presence of a large excess of one ligand (C_3E_6D, K_5CNH_2, or MUTAB), the GSH NC suspension was purified by size exclusion ultracentrifugation to remove the free ligands and the glutathione excess to isolate the corresponding NCs. After C_3E_6D ligand exchange, the emission of C_3E_6D AuNCs remains at 620 nm but the excitation varies due to the ligand exchange on the surface, going from 430 to 380 nm.[33] The presence of the PEG, in addition to increasing the colloidal stability of AuNCs, can increase its fluorescence intensity (Figure S4a,b), in agreement with previous reports in the case of thiol PEGylated ligand,[34] by increasing the fluorescence quantum yield (3% for GSH AuNCs and 6% after C_3E_6D ligand exchange). This observation may be attributed to the rigidification of the external shell permitting a decrease in energy loss due to intramolecular vibrations and rotations.[35,36] The C_3E_6D AuNCs were kept in solution without any aggregation for one year, and the fluorescence remained almost constant for 120 days (Figure S4c,d). The FT-IR spectra of purified C_3E_6D AuNCs and GSH AuNCs have been recorded, as those of C_3E_6D and GSH alone (Figure S5a,b). The two ligands exhibit two peaks assigned to amide II and amide I bonds at 1540 and 1650 cm^{-1}, respectively. The presence of C_3E_6D is confirmed by the two peaks assigned to the methylene vibrations at 2922 and 2850 cm^{-1}, respectively, that are absent in the case of GSH alone. The same ligand exchange was successfully performed with the C_5PEG_4 negatively charged derivative bearing an additional undecyl chain as a hydrophobic spacer between the tricystein anchor and the PEG hydrophilic part. Positively charged NCs were prepared with the positively charged K_5CNH_2 or MUTAB compound (Figure S3). Thus, this synthesis that includes the ligand exchange step allows us to obtain AuNCs of various surface charges that are stable against aggregation in water, biocompatible, and fluorescent with an emission wavelength of 620 nm fixed by the nanocluster size.

Due to their ultrasmall size, these biocompatible nanostructures could label lipidic biomembranes. From this perspective, we investigate the interaction of these gold nanoclusters with model membranes and EVs from follicular human fluid and how modification of their surface properties influences this interaction. With this view, large unilamellar vesicles (LUVs, ∼100 nm of diameter) were synthesized by extrusion and their size distribution was measured by dynamic light scattering (DLS) (Figure S6). The positively charged (9:1 DOPC/DOTAP) vesicles were made to interact with the negatively (C_3E_6D AuNCs or C_5PEG_4 AuNCs) and positively charged NCs (K_5CNH_2 AuNCs or MUTAB AuNCs). The nanoclusters were prepared from the same batch of GSH NCs obtained by gold reduction with glutathione used previously. Only the ligand exchange step was adapted to vary the charge of the NCs (Figure 2a,b).

The titrations of the LUVs and the EVs with oppositely charged AuNCs were performed, and the surface charge evolution was followed by measuring the electrostatic ζ potential of the vesicles. In the case of oppositely charged AuNC and LUVs, the ζ potential decreases, indicating that the negatively charged NCs neutralize the positive surface charge of the liposome until charge inversion. This behavior is attributed to the saturation of the surface vesicle due to an excess of negatively charged NCs. Finally the suspension precipitated slowly after the end of the titration. As the electrostatic interaction between vesicles and AuNC results in a charge reversion of the vesicles, the AuNCs and the vesicles covered with AuNCs can further interact to form a condensed

https://doi.org/10.1021/acs.jpclett.2c01071
J. Phys. Chem. Lett. 2022, 13, 6935−6943

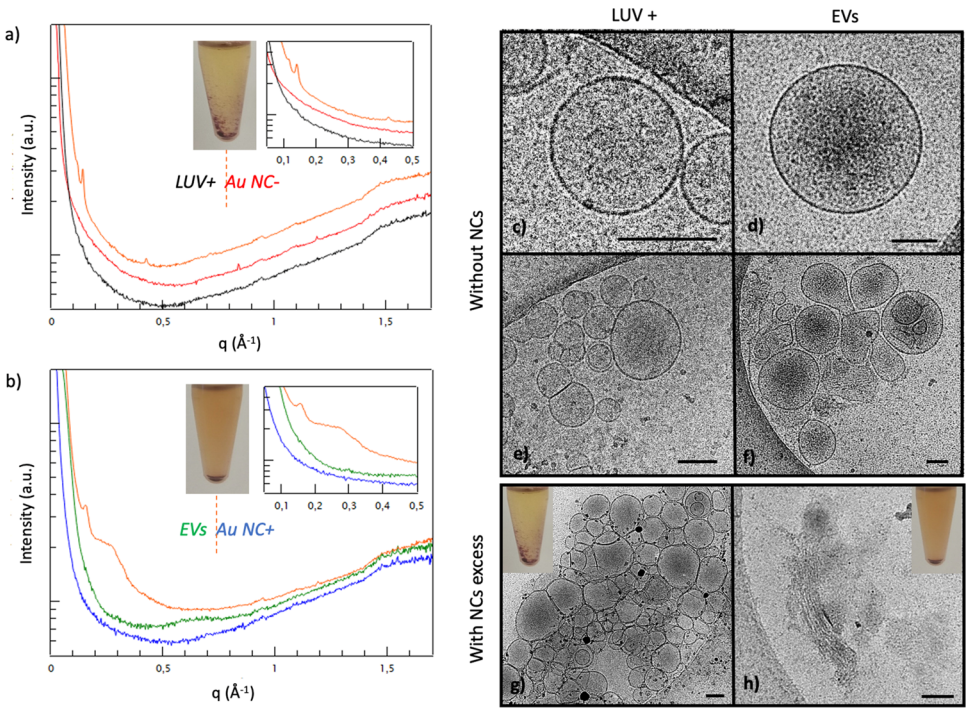

Figure 3. SAXS of the precipitate obtained at the end of the zetametry titration study of (a) LUV+ and AuNC− and (b) EVs and AuNC+ after incubation for 2 weeks: (orange) precipitate showing the appearance of two peaks, (black) LUV+, (green) EVs, (red) AuNC−, and (blue) AuNC+ alone. Cryo-TEM images (scale bar, 100 nm) of (c, e, and g) LUV+ and (d, f, and h) EVs at different magnifications without AuNCs (c−f) and with an excess of C_3E_6D AuNC− (g and h) at the end of the zetametry titration.

precipitate stabilized by electrostatic forces as observed in the case of DNA macromolecules or quantum dots and cationic lipids.[15] As a control experiment, in the presence of positively charged NCs (MUTAB AuNCs), an initial increase in the ζ potential from 15 to 40 mV is observed due to the additional contribution of the positively charged AuNCs to the mean ζ potential. When the amount of AuNCs increases, there is no further variation of the ζ potential and no final precipitation, suggesting that the NCs and the vesicles keep their surface charge, the repulsive electrostatic forces preventing colloidal instability (Figure 2c). Similar results were obtained by titration of positively charged liposomes with negatively charged C_5PEG_4 NCs or positively charged K_5CNH_2 NCs (Figure S7).

The same titrations were performed with EVs extracted from follicular liquid. As previously observed for liposomes, the negative surface charge of the exosomes was decreased by interaction with oppositely charged nanoclusters (MUTAB AuNCs) until reaching a plateau whereas no variation was observed for the surface charge in the presence of equally charged nanoclusters, C_3E_6D NCs (Figure 2d). As a charge reversion was observed during the titration of both liposomes and exosomes, a clear interaction between the lipidic membranes through electrostatics is demonstrated, resulting in a precipitation after charge reversion.

The precipitates were analyzed by two complementary techniques to investigate in situ the structuring of mixtures of nanoparticles and lipidic membranes.[16,15] SAXS (small-angle X-ray scattering) of the final precipitate obtained starting from the LUV reveals the signature of a lamellar structure (see Figure 3a). Under the cryo-TEM microscopy conditions, it is noticeable that the AuNC are difficult to detect together with the vesicles. We focus then the analysis of the vesicle membranes. The corresponding cryo-TEM images of the LUVs alone (Figure 3c,e) and the final precipitate (Figure 3g) reveal the presence of strongly adhered vesicles in the precipitate induced by the presence of the AuNCs. In the case of the EVs, SAXS shows the appearance of two broad peaks corresponding to a lamellar phase (Figure 3b), which is confirmed by cryo-TEM images of EVs alone (Figure 3d,f) and the corresponding precipitates (Figure 3h). Almost all of the EVs have been disrupted to form a condensed lamellar phase, whereas the synthetic vesicles remain only aggregated and adhered without disruption of the vesicular membrane.

A complementary analysis was performed by SAXS to follow the formation of the lamellar phase. The X-ray capillaries (diameter of 1.5 mm) were filled with a 9:1 DMPC/DMTAP solution of SUV+, and then the suspensions of C_3E_6D AuNC− or MUTAB AuNC+ were added in large excess on the top to create a contact surface between the two suspensions. Due to the lipid concentration required for SAXS experiments, small unilamellar vesicles (SUVs) with diameters of ∼50 nm (Figure S6c,d) were prepared by sonication from a lipid mixture at a higher concentration (20 mg/mL) following well-known protocols.[15] The capillaries were held at room temperature for 48 h to allow self-diffusion of AuNC and SUV+. The obtained SAXS spectra recorded at different heights in the capillary confirm the transition from a lamellar lipidic phase corresponding to SUV+ alone with two peaks at 0.08 and 0.16 $Å^{-1}$ to a hybrid phase in the presence of AuNC− with two peaks at 0.07 and 0.13 $Å^{-1}$ (Figure S8a), whereas no such transition was observed in the case of AuNC+ (Figure S8b). In the case of neutral DMPC SUVs, the presence of AuNCs does not induce such behavior (Figure S8c,d). In all of the cases presented here, via wide-angle X-ray scattering analysis it is noteworthy that the lipid chains remain crystalline even in the

https://doi.org/10.1021/acs.jpclett.2c01071
J. Phys. Chem. Lett. 2022, 13, 6935−6943

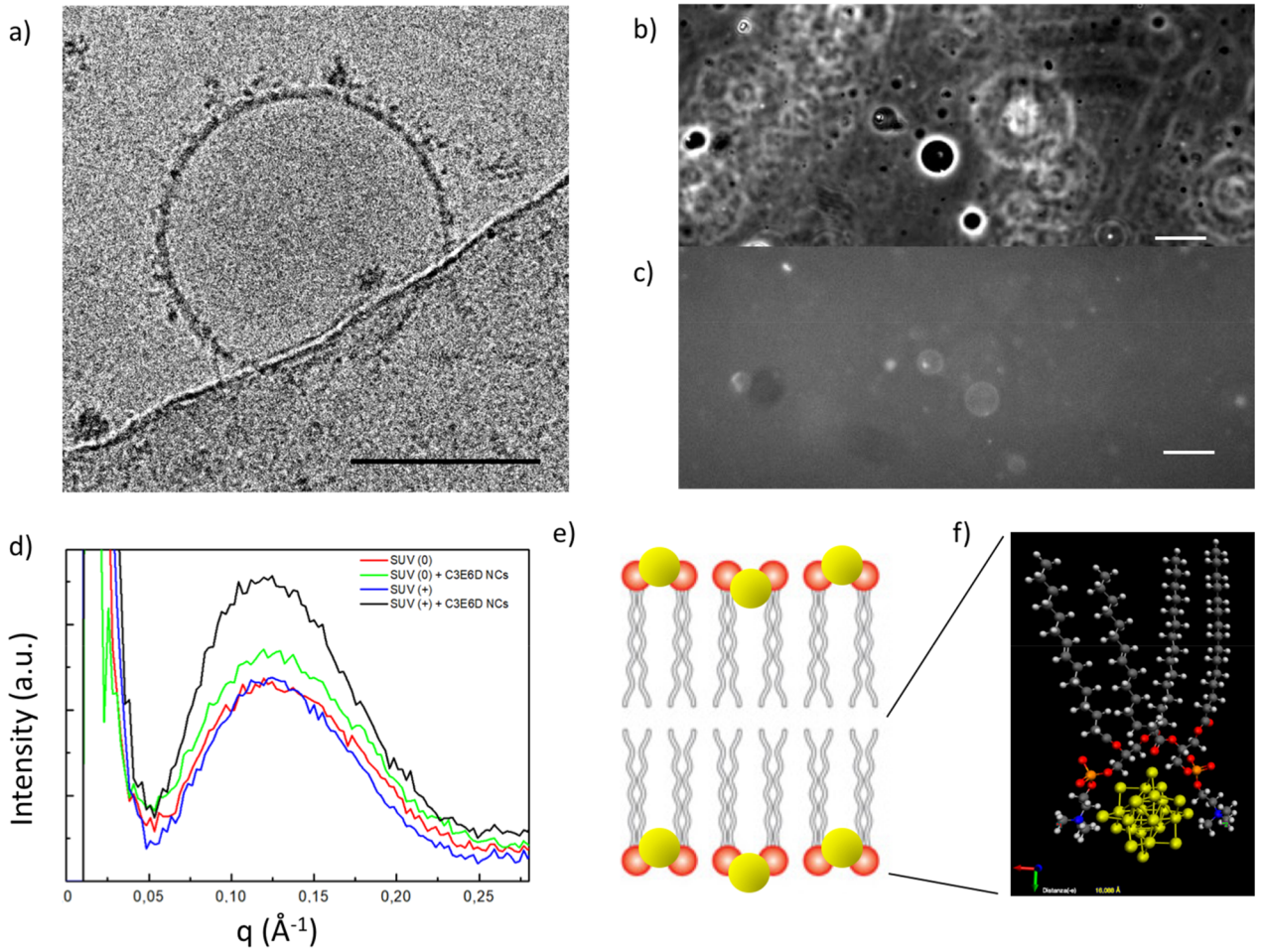

Figure 4. (a) Cryo-TEM images (scale bar, 100 nm) of LUV+ incubated with of C_3E_6D AuNC−. Optical microscopy images (scale bar, 50 μM) of GUV+ (giant unilamellar vesicles) interacting with C_3E_6D AuNC− obtained (b) by phase contrast and (c) by fluorescence. (d) SAXS spectra of 9:1 DMPC/DMTAP positively charged unilamellar SUV+ alone (blue) or in the presence of C_3E_6D AuNC− (black) and SAXS spectra of DMPC unilamellar SUV alone (red) or in the presence of a suspension of C_3E_6D AuNC− (green). (e) Schematic view and (f) Avogadro simulation of AuNCs positioned between the polar heads of membrane phospholipids in the case of electrostatic attraction.

presence of the NCs. This later observation indicates that the chain melting phase transition of the DMPC/DMTAP mixture is not lowered by the NC interactions. This has already been observed with electrostatic interactions of DNA, for which the melting temperature is increased by a few degrees Celsius.[37] This is explained by weakening of the repulsion of the cationic TAP headgroup due to new polyanion absorption. The same SAXS experiments were performed with EVs from human follicular fluid. As the exosome membrane presents a complex composition, the spectra do not exhibit a clear diffraction peak corresponding to the lamellar lipidic packing (Figure S9). As controls, MUTAB solutions of various concentrations in the presence or absence of EVs do not present any diffraction peak, so that the MUTAB ligand itself is not involved in the change in the spectrum of SAXS EVs (Figure S10). A slight increase in intensity was observed in the range of 0.15 $Å^{-1}$ only in the case of the Au NC+, which is attributed to the presence of the NCs at the bilayer surface of the EVs (Figure S9b). In conclusion, the cryo-TEM images and the SAXS measurements permit the observation that the strong electrostatic interaction between nanoclusters and vesicles results in the formation of a hybrid lamellar phase composed of the lipid membranes and the NCs.

The cryo-TEM images exhibit black points of strong electron density in the vicinity of the oppositively charged membranes of LUVs that could be attributed to the presence of AuNCs (Figure 4a). To confirm this observation, the fluorescence properties of AuNCs were then exploited to visualize them at the surface of vesicles. Giant unilamellar vesicles (GUVs) with diameters in the micrometer range were synthesized according to the water-in-oil emulsion transfer methods[38] and incubated in the presence of the NCs. The positively charged GUVs in excess were incubated for 1 h in the presence of C_3E_6D NCs (negatively charged) and then visualized under a fluorescence optical microscope, which allowed us to see the location of the fluorescent AuNCs. The fluorescence is localized on the surface of GUVs (Figure 4b,c), indicating that the AuNCs were attracted to the opposite charge of the GUV membrane during the incubation as already observed in the case of quantum dots.[15] These two experiments suggest that the nanoclusters are adhering to the membranes in agreement with the progressive neutralization of the surface charge observed by zetametry. In light of the precise position of the AuNC nanostructures on the membrane, all of the samples were analyzed by SAXS after equilibration of the resulting structures. A scattering peak at 0.122 $Å^{-1}$ corresponding to the expected membrane thickness

https://doi.org/10.1021/acs.jpclett.2c01071
J. Phys. Chem. Lett. 2022, 13, 6935−6943

of the SUVs (5.1 nm) was observed and was enhanced in the presence of oppositely charged NCs (Figure 4d). The highest intensity peak occurs for C_3E_6D AuNC− that strongly interact with 9:1 DMPC/DMTAP SUV+. This increase in the intensity of the scattering signal is attributed to the increasing number of AuNCs adhering electrostatically to the membrane. The observed intensity enhancement is attributed to the high gold atomic number that, with an increase in the X-ray scattering contrast, also increases the intensity of the signal on the SAXS spectrum. One can also notice a slight increase of the intensity peak with the DMPC SUV(0) that are slightly negatively charged due to the orientation of the phosphatidylcholine headgroup dipole with a mean ζ potential of ∼10 mV.[39] A final important point is that, although the AuNCs are positioned on the membrane, enhancing the SAXS signal, there is no shift in the peak when the vesicles are in excess. This indicates that NCs do not vary the thickness of the membrane and, due to their ultrasmall size, manage to insert themselves between the polar heads of the membrane phospholipids (Figure 4e) without increasing the bilayer thickness as opposed to other larger nanoparticles such as quantum dots.[15−17] An Avogadro simulation was performed as a rough estimation to evaluate if the NC size permits them to insert at the level of the phosphate headgroup. A comparison of phosphate headgroup distances with and without NCs is also shown schematically in Figure S11, indicating that the AuNCs could be located at the level of phosphate groups.

In conclusion, this study gives an overview of the interaction between ultrasmall luminescent gold nanoclusters and lipidic membranes through electrostatic attraction, showing that it is possible to induce a large change in membrane structures or not. The syntheses of aqueous bioactivatable and PEGylated AuNC suspensions of various charges were performed according to a two-step process. The first step consists of the GSH AuNCs prepared in only 2 h with a dimension of ∼2 nm, with a fluorescence excitation peak at 430 nm and an emission peak at 620 nm. Then a ligand exchange step allowed binding of the AuNCs with thiol groups of different ligands to functionalize them. Following incubation of the AuNCs with oppositely charged vesicles, either liposomes or EVs, the strong electrostatic attraction resulting in the adsorption of AuNCs to the membranes was evidenced by complementary techniques such as zetametry, fluorescence optical microscopy, SAXS, and cryo-TEM. In the presence of an excess of oppositely charged AuNCs, the liposomes strongly adhere to each other without disrupting their membrane structure whereas the EVs extracted from human follicular fluid rearrange into a hybrid lamellar phase. Instead, in the presence of a membrane surface excess, AuNCs do not change the size of the membrane thickness, so they are positioned between the polar headgroups of the membrane phospholipids differently from larger gold nanoparticles.[17]

For this reason, they are promising candidates for fluorescent in vivo biosensing and biolabeling upon exploitation of their long fluorescence lifetime and high quantum yields. We are currently exploring their in vivo targeting ability because of specific recognition groups and biosensing by fluorescence because of their sensitiviy to pH and oxygen. Thanks to their ultrasmall size, these probes are easily internalized into cells and in vivo organisms. We are also currently exploring their encapsulation within synthetic vesicles for drug delivery by increasing the level of internalization and decreasing the level of nonspecific interactions. As opposed to larger gold nanoparticles, the smaller size of AuNCs not only prevents the deformation of biological membranes but also allows labeling with higher spatial resolution. Therefore, these ultrasmall and stable gold nanoclusters, by controlling their interaction with lipid membranes, can serve as a new hybrid vector for bioimaging and for in situ biosensing or drug delivery.

EXPERIMENTAL METHODS

General. Human ovarian follicular liquid samples were provided by the Biobank GERMETHEQUE. The PEGylated ligands were prepared and purchased from Agentide (HPLC purity of 85.624%). All of the other chemical compounds and solvents were purchased from Sigma-Aldrich. The measurements of the mean hydrodynamic diameters were recorded at an angle of 173° using a Nanosizer ZEN3600 (Malvern Instruments) and 25 °C, without dilution or filtration. The absorption spectra were recorded on a Thermo Scientific NanoDrop ultraviolet−visible spectrometer. The absolute fluorescence quantum yields were measured using a model C9920-03 Hamamatsu system by exciting the samples at 410 nm.

Synthesis of Au Nanoclusters (AuNCs). All glassware used for these syntheses was cleaned in a bath of freshly prepared aqua regia (HCl/HNO_3, 3:1 by volume) and rinsed in water 10 times before use. The obtained solution of AuNCs could be stored at 4 °C for months without a significant change in its optical properties. A freshly prepared aqueous solution of glutathione (denoted GSH, 50 mM, 1.2 mL) was mixed with 16.8 mL of ultrapure water. The solution was heated in an oil bath at 120 °C, and $HAuCl_4$ (20 mM, 2 mL) was rapidly added. The reaction was stopped after the mixture had been stirred for 3 h. An aqueous suspension of orange-emitting GSH AuNCs was formed (2.6 μM). Then a freshly prepared aqueous solution of the desired ligand (20 mM, 1000 equiv/Au) (C_3E_6D, K_5CNH_2, or MUTAB) was incubated overnight in the presence of the GSH AuNCs. The obtained AuNCs were purified on a centrifugal filter (Amicon-ultra 0.5 device 3 kDa, Merk) to remove the excess of the ligand. Typically, a freshly prepared aqueous solution of C_3E_6D (20 mM, 0.390 mL) was incubated overnight with a suspension of GSH Au NCs (2.6 μM, 1 mL) in the dark at room temperature to obtain the final C_3E_6D AuNCs (denoted AuNC−).

Preparation of Phospholipidic Vesicles (GUVs, LUVs, and SUVs). Large Unilamellar Vesicles (LUVs). Lipidic stock solutions of DOPC (1 mL, 10 mg/mL) and DOTAP (98.5 μL, 10 mg/mL) in dichloromethane were prepared. The appropriate lipidic mixture (total lipid concentration of 10 mg/mL), either pure DOPC or a molar 9:1 DOPC/DOTAP mixture, was introduced into a 50 mL vial, and the organic solvent was evaporated with a rotary evaporator (Büchi Heating Bath) (40 °C, 100 mbar) to form a lipidic film on the vial surface during 30 min. Then, an aqueous sucrose solution (1.2 mL, 50 mM) was added, and the suspension was successively placed in a liquid nitrogen bath for 30 s and in a water bath at 40 °C for 30 s. The freezing−unfreezing cycle was repeated five times to form the MLVs (multilamellar vesicles). This MLV suspension was then extruded 10 times through a 100 nm diameter polycarbonate filter in an extruder (Thermobarrel Extruder Lipex Membrane) under a pressure of 10−15 bar. The mean hydrodynamic diameter of the obtained LUVs was measured to be around 110 ± 20 nm by DLS (Figure S5a,b).

https://doi.org/10.1021/acs.jpclett.2c01071
J. Phys. Chem. Lett. 2022, 13, 6935−6943

Small Unilamellar Vesicles (SUVs). A lipid solution was prepared by dissolving 20 mg of DMPC and 1.74 mg of DMTAP in 2 mL of dichloromethane. Using a rotary evaporator (Buchi Heating Bath), the dichloromethane was evaporated (40 °C, 100 mbar) and an aqueous sucrose solution (2 mL, 50 mM) was added to hydrate the as-formed lipidic film. The obtained solution was sonicated using a titanium ultrasonic probe (Misonix Inc.) placed at maximum power for 30 min. After centrifugation at 7500*g* for 10 min to eliminate the possible titanium traces, the supernatant was then removed and the SUV solution was ready for use. The average size of the SUVs estimated by DLS was 46 ± 16 nm (Figure S5c,d).

Giant Unilamellar Vesicles (GUVs).[38] A lipid solution was prepared by dissolving DOPC or a molar 95:5 DOPC/DOTAP lipidic mixture in chloroform (10 mg/mL). Twenty microliters of this solution and 1.8 mL of paraffin oil were mixed and heated at 80 °C for 30 min in a flask without a cap. Then, the suspension was placed in a desiccator for 20 min to evaporate the chloroform and to obtain the final lipid organic solution. To prepare the GUVs, 50 μL of sucrose (500 mM) was added to 400 μL of the lipid solution vortexed for 40 s to form a water-in-oil (w/o) emulsion. Then, this emulsion was gently added on the top of a sucrose solution of high viscosity (200 μL, 500 mM in a second Eppendorf tube) without mixing. After waiting 10 min, the solution was centrifuged for 15 min at 18890*g*. The bottom was transferred into another Eppendorf tube, redispersed in 300 μL of glucose (500 mM), and centrifuged again at 18890*g* for 5 min. After centrifugation, the bottom solution was taken up and the GUVs were ready to be stored in the refrigerator.

Small-Angle X-ray Scattering (SAXS). X-ray patterns were collected with a Mar345 Image-Plate detector (Maresearch, Norderstedt, Germany) mounted on a rotating anode X-ray generator (FR591, Bruker, Courtaboeuf, France) operated at 50 kV and 50 mA. The sample−detector distance (422 mm) has been calibrated by using silver behenate. The X-ray patterns were therefore recorded for a range of reciprocal spacing $q = 4\pi \sin\theta/\lambda$ from 0.04 to 1.2 Å^{-1}, where θ is the diffraction angle. The experiments performed with this setup provided accurate measurements of distances between 150 and 5.2 Å. The acquisition time was 1 h. Samples were loaded in thin Lindman glass capillaries [diameter of 1 ± 0.1 mm and thickness of 10 μm (GLAS, Muller, Berlin, Germany)] sealed with paraffin. The lipid−NC hybrid complexes were prepared by mixing a micromolar solution of NCs (10 μL, 1.70 μM NCs) and a millimolar suspension of SUVs (10 μL, total phospholipid concentration of 16 mM) in the glass capillaries. All samples exhibited powder diffraction rings, and the scattering intensities as a function of the radial wave vector were determined by circular integration.

ζ Potential Measurements. The ζ potential measurements were performed using the Zetasizer ZEN3600 (Malvern Instruments) equipped with a He−Ne laser source (λ = 633 nm). Millimolar solutions of vesicles were loaded into disposable folded capillary cells (Zeta Cell, DTS 1060), and data were collected at 25 °C. A 3 mM vesicle solution was diluted three times with 25 mM NaCl to give a 1 mM vesicle solution. Its ζ potential was measured, and then a few microliters of NCs (8.7 μM diluted three times with 25 mM NaCl) was added little by little via titration; the ζ potential was measured after each addition. The ζ potential of the vesicles was extracted from the inelastic scattering frequency shift of the laser signal scattered by moving the charged colloid under an electric field (applied cell voltage of 15 V).

Spectrofluorimetry. Photoluminescence measurements were performed on a Jasco FP-8300 spectrofluorometer. The measurements were performed at room temperature on liquid samples. The wavelength resolution of the excitation and emission slits was set to 5 nm. The response times was 0.5 s. The detector sensitivity was set to medium, and the scan speed was 500 nm/min.

Luminescence Lifetime Measurements. Luminescence measurements were performed by pumping with the 325 nm line of a HeCd laser. The pump power was 0.6 mW over a circular area with a diameter of 1 mm, and the laser beam was chopped through an acousto-optic modulator at a frequency of 55 Hz. The luminescence signal was analyzed by a single-grating monochromator and detected by a photomultiplier tube. Luminescence lifetime measurements were performed by detecting the luminescence signal at 600 nm after pumping to the steady state, switching off the laser beam, and analyzing it with a photon counting multichannel scaler having the signal from the modulator as a trigger.

Light Optical Microscopy. The fluorescence optical microscopy observations were made under direct bright light and epifluorescence on an inverted microscope (IX71, Olympus) equipped with 20×, 0.45 (NA) objectives (Olympus). Solutions of NCs were excited at 365 nm by a high-vacuum mercury lamp (200 W). Images were acquired by a Photometrics CoolSNAP HQ2 camera equipped with a soft imaging system (Olympus).

Transmission Electron Microscopy (TEM). TEM analyses were carried out with a JEOL 2100 transmission electron microscope operated at 200 kV supplied with an UltraScan 1000XP CCD Camera. For sample preparation, 300 mesh carbon-coated nickel grids were placed for 1 min on top of a 40 μL sample droplet and dried with paper. Particle sizes and interparticle distances were determined from TEM micrographs using Fiji Software.

Cryo-Transmission Electron Microscopy (cryo-TEM). Vitrification of vesicles was performed using an automatic plunge freezer (EM GP, Leica) at controlled humidity and temperature (Dubochet and McDowall, 1981). The samples were deposited onto glow-discharged electron microscope grids followed by blotting and vitrification by rapid freezing in liquid ethane. Grids were transferred to a single-axis cryo-holder (model 626, Gatan) and observed using a 200 kV electron microscope (Tecnai G^2 T20 Sphera, FEI) equipped with a 4K × 4K CCD camera (XF416, TVIPS). Micrographs were acquired under small electron doses using the camera in binning mode 1 and at a nominal magnification of 25000×.

■ ASSOCIATED CONTENT

Supporting Information

The Supporting Information is available free of charge at https://pubs.acs.org/doi/10.1021/acs.jpclett.2c01071.

Fluorescence spectra, fluorescence lifetimes, and size distribution histogram of AuNCs (Figure S1); image of lyophilized AuNCs (Figure S2); chemical structures of AuNC ligands (Figure S3); excitation and emission intensity spectra of AuNCs before and after ligand exchange and purification, DLS, and fluorescence spectrum showing the stability of AuNCs after 4 months (Figure S4); FT-IR spectra of purified C_3E_6D AuNCs

https://doi.org/10.1021/acs.jpclett.2c01071
J. Phys. Chem. Lett. 2022, 13, 6935−6943

and GSH AuNCs as well as C_3E_6D and GSH alone (Figure S5); DLS measurements of LUVs and SUVs (Figure S6); ζ potential titration of LUV+ with K_5CNH_2 and C_5PEG_4 AuNCs (Figure S7); SAXS spectra of SUV + and DMPC SUV interacting with Au NC+ or Au NC− (Figure S8); SAXS spectra of EVs interacting with Au NC+ or Au NC− (Figure S9); SAXS of MUTAB with or without EVs (Figure S10); and Avogadro simulation of AuNCs interacting with membrane phospholipids (Figure S11) (PDF)

Transparent Peer Review report available (PDF)

AUTHOR INFORMATION

Corresponding Author

Valérie Marchi − *Université Rennes 1, CNRS UMR 6226, Institut des Sciences Chimiques de Rennes, 35042 Rennes, France;* orcid.org/0000-0002-6565-7201; Email: valerie.marchi@univ-rennes1.fr

Authors

Regina M. Chiechio − *Université Rennes 1, CNRS UMR 6226, Institut des Sciences Chimiques de Rennes, 35042 Rennes, France; Dipartimento di Fisica e Astronomia "Ettore Majorana", Università Di Catania, 95123 Catania, Italy; IMM-CNR, 95123 Catania, Italy*

Solène Ducarre − *Université Rennes 1, CNRS UMR 6226, Institut des Sciences Chimiques de Rennes, 35042 Rennes, France*

Grégory Moulin − *Université Rennes 1, CNRS UMR 6226, Institut des Sciences Chimiques de Rennes, 35042 Rennes, France; CHU Rennes, Service de Biologie de la Reproduction-CECOS, 35000 Rennes, France*

Aurélien Dupont − *CNRS, Inserm, BIOSIT - UMS 3480, Univ Rennes, US_S 018, F-35000 Rennes, France*

Célia Marets − *Université Rennes 1, CNRS UMR 6226, Institut des Sciences Chimiques de Rennes, 35042 Rennes, France;* orcid.org/0000-0002-5670-1020

Pascale Even-Hernandez − *Université Rennes 1, CNRS UMR 6226, Institut des Sciences Chimiques de Rennes, 35042 Rennes, France*

Franck Artzner − *Université Rennes 1, CNRS UMR 6251, Institut de Physique de Rennes, 35042 Rennes, France*

Paolo Musumeci − *Dipartimento di Fisica e Astronomia "Ettore Majorana", Università Di Catania, 95123 Catania, Italy*

Giorgia Franzò − *IMM-CNR, 95123 Catania, Italy;* orcid.org/0000-0003-3630-0315

Célia Ravel − *CHU Rennes, Service de Biologie de la Reproduction-CECOS, 35000 Rennes, France; Univ Rennes, Inserm, EHESP, Irset (Institut de Recherche en Santé, Environnement et Travail), F-35000 Rennes, France*

Maria José LoFaro − *Dipartimento di Fisica e Astronomia "Ettore Majorana", Università Di Catania, 95123 Catania, Italy; IMM-CNR, 95123 Catania, Italy*

Complete contact information is available at: https://pubs.acs.org/10.1021/acs.jpclett.2c01071

Notes

The authors declare no competing financial interest.

ACKNOWLEDGMENTS

The authors thank La Ligue Contre le Cancer for financial support. The authors also thank Catania University for a fellowship to R.M.C. and Rennes1 University for its fellowship to S.D. The authors are grateful to V. Dorcet for the assistance with the TEM experiments performed on the THEMIS platform and G. Taupier for the assistance with the quantum yield measurements performed on the Caphter platform (ScanMAT, UAR 2025 University of Rennes 1-CNRS; CPER-FEDER 2007−2014).

REFERENCES

(1) Wang, J.; Ye, J.; Jiang, H.; Gao, S.; Ge, W.; Chen, Y.; Liu, C.; Amatore, C.; Wang, X. Simultaneous and Multisite Tumor Rapid-Target Bioimaging through in Vivo Biosynthesis of Fluorescent Gold Nanoclusters. *RSC Adv.* **2014**, *4* (71), 37790−37795.

(2) Nonappa. Luminescent Gold Nanoclusters for Bioimaging Applications. *Beilstein J. Nanotechnol.* **2020**, *11* (1), 533−546.

(3) Cui, H.; Shao, Z.-S.; Song, Z.; Wang, Y.-B.; Wang, H.-S. Development of Gold Nanoclusters: From Preparation to Applications in the Field of Biomedicine. *J. Mater. Chem. C* **2020**, *8* (41), 14312−14333.

(4) Zhang, X.-D.; Luo, Z.; Chen, J.; Song, S.; Yuan, X.; Shen, X.; Wang, H.; Sun, Y.; Gao, K.; Zhang, L.; Fan, S.; Leong, D. T.; Guo, M.; Xie, J. Ultrasmall Glutathione-Protected Gold Nanoclusters as Next Generation Radiotherapy Sensitizers with High Tumor Uptake and High Renal Clearance. *Sci. Rep.* **2015**, *5* (1), 8669.

(5) Loynachan, C. N.; Soleimany, A. P.; Dudani, J. S.; Lin, Y.; Najer, A.; Bekdemir, A.; Chen, Q.; Bhatia, S. N.; Stevens, M. M. Renal Clearable Catalytic Gold Nanoclusters for in Vivo Disease Monitoring. *Nat. Nanotechnol.* **2019**, *14* (9), 883−890.

(6) Zhang, X.-D.; Wu, D.; Shen, X.; Liu, P.-X.; Fan, F.-Y.; Fan, S.-J. In Vivo Renal Clearance, Biodistribution, Toxicity of Gold Nanoclusters. *Biomaterials* **2012**, *33* (18), 4628−4638.

(7) Liang, G.; Jin, X.; Zhang, S.; Xing, D. RGD Peptide-Modified Fluorescent Gold Nanoclusters as Highly Efficient Tumor-Targeted Radiotherapy Sensitizers. *Biomaterials* **2017**, *144*, 95−104.

(8) Tao, Y.; Li, M.; Kim, B.; Auguste, D. T. Incorporating Gold Nanoclusters and Target-Directed Liposomes as a Synergistic Amplified Colorimetric Sensor for HER2-Positive Breast Cancer Cell Detection. *Theranostics* **2017**, *7* (4), 899−911.

(9) Chen, L.-Y.; Wang, C.-W.; Yuan, Z.; Chang, H.-T. Fluorescent Gold Nanoclusters: Recent Advances in Sensing and Imaging. *Anal. Chem.* **2015**, *87* (1), 216−229.

(10) Porret, E.; Sancey, L.; Martín-Serrano, A.; Montañez, M. I.; Seeman, R.; Yahia-Ammar, A.; Okuno, H.; Gomez, F.; Ariza, A.; Hildebrandt, N.; Fleury, J.-B.; Coll, J.-L.; Le Guével, X. Hydrophobicity of Gold Nanoclusters Influences Their Interactions with Biological Barriers. *Chem. Mater.* **2017**, *29* (17), 7497−7506.

(11) Chatterjee, A.; Purkayastha, P. The Impact of Lipid Head-Groups in GUVs on Electron Transfer by Surface-Adsorbed Fluorescent Gold Nanoclusters. *Mater. Adv.* **2021**, *2* (4), 1343−1350.

(12) Porret, E.; Fleury, J.-B.; Sancey, L.; Pezet, M.; Coll, J.-L.; Le Guével, X. Augmented Interaction of Multivalent Arginine Coated Gold Nanoclusters with Lipid Membranes and Cells. *RSC Adv.* **2020**, *10* (11), 6436−6443.

(13) Porret, E.; Le Guével, X.; Coll, J.-L. Gold Nanoclusters for Biomedical Applications: Toward *in Vivo* Studies. *J. Mater. Chem. B* **2020**, *8* (11), 2216−2232.

(14) Kauscher, U.; Penders, J.; Nagelkerke, A.; Holme, M. N.; Nele, V.; Massi, L.; Gopal, S.; Whittaker, T. E.; Stevens, M. M. Gold Nanocluster Extracellular Vesicle Supraparticles: Self-Assembled Nanostructures for Three-Dimensional Uptake Visualization. *Langmuir* **2020**, *36* (14), 3912−3923.

(15) Dif, A.; Henry, E.; Artzner, F.; Baudy-Floc'h, M.; Schmutz, M.; Dahan, M.; Marchi-Artzner, V. Interaction between Water-Soluble Peptidic CdSe/ZnS Nanocrystals and Membranes: Formation of

Hybrid Vesicles and Condensed Lamellar Phases. *J. Am. Chem. Soc.* **2008**, *130* (26), 8289−8296.
(16) Bizien, T.; Ameline, J.-C.; Yager, K. G.; Marchi, V.; Artzner, F. Self-Organization of Quantum Rods Induced by Lipid Membrane Corrugations. *Langmuir* **2015**, *31* (44), 12148−12154.
(17) Contini, C.; Hindley, J. W.; Macdonald, T. J.; Barritt, J. D.; Ces, O.; Quirke, N. Size Dependency of Gold Nanoparticles Interacting with Model Membranes. *Commun. Chem.* **2020**, *3* (1), 130.
(18) Hung, W.-T.; Navakanitworakul, R.; Khan, T.; Zhang, P.; Davis, J. S.; McGinnis, L. K.; Christenson, L. K. Stage-Specific Follicular Extracellular Vesicle Uptake and Regulation of Bovine Granulosa Cell Proliferation†. *Biol. Reprod.* **2017**, *97* (4), 644−655.
(19) Yefimova, M. G.; Béré, E.; Cantereau-Becq, A.; Meunier-Balandre, A.-C.; Merceron, B.; Burel, A.; Merienne, K.; Ravel, C.; Becq, F.; Bourmeyster, N. Myelinosome Organelles in the Retina of R6/1 Huntington Disease (HD) Mice: Ubiquitous Distribution and Possible Role in Disease Spreading. *Int. J. Mol. Sci.* **2021**, *22* (23), 12771.
(20) Neyroud, A.-S.; Chiechio, R.; Yefimova, M.; Lo Faro, M. J.; Dejucq-Rainsford, N.; Jaillard, S.; Even-Hernandez, P.; Marchi, V.; Ravel, C. Extra-Cellular Vesicles of the Male Genital Tract: New Actors in Male Fertility? *Basic and Clinical Andrology* **2021**, *31* (1), 25.
(21) Bourmeyster, N. Myelinosome-Driven Secretion: Non-Catabolic Management of Misfolded Proteins - Lessons from the Sertoli Cells. *J. Rare Dis. Res. Treat.* **2017**, *2* (2), 24−27.
(22) Yefimova, M. G.; Béré, E.; Cantereau-Becq, A.; Harnois, T.; Meunier, A.-C.; Messaddeq, N.; Becq, F.; Trottier, Y.; Bourmeyster, N. Myelinosomes Act as Natural Secretory Organelles in Sertoli Cells to Prevent Accumulation of Aggregate-Prone Mutant Huntingtin and CFTR. *Hum. Mol. Genet.* **2016**, *25* (19), 4170−4185.
(23) Beach, A.; Zhang, H.-G.; Ratajczak, M. Z.; Kakar, S. S. Exosomes: An Overview of Biogenesis, Composition and Role in Ovarian Cancer. *J. Ovarian Res.* **2014**, *7* (1), 14.
(24) Bai, Y.; Lu, Y.; Wang, K.; Cheng, Z.; Qu, Y.; Qiu, S.; Zhou, L.; Wu, Z.; Liu, H.; Zhao, J.; Mao, H. Rapid Isolation and Multiplexed Detection of Exosome Tumor Markers Via Queued Beads Combined with Quantum Dots in a Microarray. *Nano-Micro Lett.* **2019**, *11* (1), 59.
(25) Cheng, J.; Nonaka, T.; Wong, D. Salivary Exosomes as Nanocarriers for Cancer Biomarker Delivery. *Materials* **2019**, *12* (4), 654.
(26) Luo, Z.; Yuan, X.; Yu, Y.; Zhang, Q.; Leong, D. T.; Lee, J. Y.; Xie, J. From Aggregation-Induced Emission of Au(I)-Thiolate Complexes to Ultrabright Au(0)@Au(I)-Thiolate Core-Shell Nanoclusters. *J. Am. Chem. Soc.* **2012**, *134* (40), 16662−16670.
(27) Gurunatha, K. L.; Fournier, A. C.; Urvoas, A.; Valerio-Lepiniec, M.; Marchi, V.; Minard, P.; Dujardin, E. Nanoparticles Self-Assembly Driven by High Affinity Repeat Protein Pairing. *ACS Nano* **2016**, *10* (3), 3176−3185.
(28) Piñeiro, Y.; Rivas, J.; López-Quintela, M. A. The Emergence of Quantum Confinement in Atomic Quantum Clusters. In *Colloidal Foundations of Nanoscience*; Elsevier, 2014; pp 81−105.
(29) Huang, Y.; Fuksman, L.; Zheng, J. Luminescence Mechanisms of Ultrasmall Gold Nanoparticles. *Dalton Trans.* **2018**, *47* (18), 6267−6273.
(30) Oh, E.; Huston, A. L.; Shabaev, A.; Efros, A.; Currie, M.; Susumu, K.; Bussmann, K.; Goswami, R.; Fatemi, F. K.; Medintz, I. L. Energy Transfer Sensitization of Luminescent Gold Nanoclusters: More than Just the Classical Förster Mechanism. *Sci. Rep.* **2016**, *6* (1), 35538.
(31) Hamon, C.; Postic, M.; Mazari, E.; Bizien, T.; Dupuis, C.; Even-Hernandez, P.; Jimenez, A.; Courbin, L.; Gosse, C.; Artzner, F.; Marchi-Artzner, V. Three-Dimensional Self-Assembling of Gold Nanorods with Controlled Macroscopic Shape and Local Smectic B Order. *ACS Nano* **2012**, *6* (5), 4137−4146.
(32) Fernandez, M.; Urvoas, A.; Even-Hernandez, P.; Burel, A.; Mériadec, C.; Artzner, F.; Bouceba, T.; Minard, P.; Dujardin, E.; Marchi, V. Hybrid Gold Nanoparticle-Quantum Dot Self-Assembled Nanostructures Driven by Complementary Artificial Proteins. *Nanoscale* **2020**, *12* (7), 4612−4621.
(33) Stamplecoskie, K. G.; Chen, Y.-S.; Kamat, P. V. Excited-State Behavior of Luminescent Glutathione-Protected Gold Clusters. *J. Phys. Chem. C* **2014**, *118* (2), 1370−1376.
(34) Oh, E.; Fatemi, F. K.; Currie, M.; Delehanty, J. B.; Pons, T.; Fragola, A.; Lévêque-Fort, S.; Goswami, R.; Susumu, K.; Huston, A. L.; Medintz, I. L. PEGylated Luminescent Gold Nanoclusters: Synthesis, Characterization, Bioconjugation, and Application to One- and Two-Photon Cellular Imaging. *Part. Part. Syst. Charact.* **2013**, *30* (5), 453−466.
(35) Pyo, K.; Thanthirige, V. D.; Kwak, K.; Pandurangan, P.; Ramakrishna, G.; Lee, D. Ultrabright Luminescence from Gold Nanoclusters: Rigidifying the Au(I)-Thiolate Shell. *J. Am. Chem. Soc.* **2015**, *137* (25), 8244−8250.
(36) Wu, Z.; Jin, R. On the Ligand's Role in the Fluorescence of Gold Nanoclusters. *Nano Lett.* **2010**, *10* (7), 2568−2573.
(37) Zantl, R.; Baicu, L.; Artzner, F.; Sprenger, I.; Rapp, G.; Rädler, J. O. Thermotropic Phase Behavior of Cationic Lipid-DNA Complexes Compared to Binary Lipid Mixtures. *J. Phys. Chem. B.* **1999**, *103*, 10300−10310.
(38) Matsushita-Ishiodori, Y.; Hanczyc, M. M.; Wang, A.; Szostak, J. W.; Yomo, T. Using Imaging Flow Cytometry to Quantify and Optimize Giant Vesicle Production by Water-in-Oil Emulsion Transfer Methods. *Langmuir* **2019**, *35* (6), 2375−2382.
(39) Disalvo, E. A.; Bouchet, A. M. Electrophoretic Mobility and Zeta Potential of Liposomes Due to Arginine and Polyarginine Adsorption. *Colloids Surf. Physicochem. Eng. Asp.* **2014**, *440*, 170−174.

https://doi.org/10.1021/acs.jpclett.2c01071
J. Phys. Chem. Lett. 2022, 13, 6935−6943